THE LARGE-SCALE COSMIC-RAY ANISOTROPY AS OBSERVED WITH MILAGRO

A. A. Abdo[1,2], B. T. Allen[3], T. Aune[4], D. Berley[5], S. Casanova[6], C. Chen[3], B. L. Dingus[6], R. W. Ellsworth[7],
L. Fleysher[8], R. Fleysher[8], M. M. Gonzalez[9], J. A. Goodman[5], C. M. Hoffman[6], B. Hopper[5], P. H. Hüntemeyer[6],
B. E. Kolterman[8], C. P. Lansdell[5], J. T. Linnemann[10], J. E. McEnery[11], A. I. Mincer[8], P. Nemethy[8], D. Noyes[5],
J. Pretz[6], J. M. Ryan[12], P. M. Saz Parkinson[4], A. Shoup[13], G. Sinnis[6], A. J. Smith[5], G. W. Sullivan[5], V. Vasileiou[5],
G. P. Walker[6], D. A. Williams[4], AND G. B. Yodh[3]

[1] National Research Council Research Associate, National Academy of Sciences, Washington, DC 20001, USA
[2] Space Science Division, Naval Research Laboratory, Washington, DC 20375, USA
[3] Department of Physics and Astronomy, University of California, Irvine, CA 92697, USA
[4] Santa Cruz Institute for Particle Physics, University of California, 1156 High Street, Santa Cruz, CA 95064, USA
[5] Department of Physics, University of Maryland, College Park, MD 20742, USA
[6] Group P-23, Los Alamos National Laboratory, P.O. Box 1663, Los Alamos, NM 87545, USA
[7] Department of Physics and Astronomy, George Mason University, 4400 University Drive, Fairfax, VA 22030, USA
[8] Department of Physics, New York University, 4 Washington Place, New York, NY 10003, USA
[9] Instituto de Astronomía, Universidad Nacional Autónoma de México, D.F., México, 04510, USA
[10] Department of Physics and Astronomy, Michigan State University, 3245 BioMedical Physical Sciences Building, East Lansing, MI 48824, USA
[11] NASA Goddard Space Flight Center, Greenbelt, MD 20771, USA
[12] Department of Physics, University of New Hampshire, Morse Hall, Durham, NH 03824, USA
[13] The Ohio State University, Lima, OH 45804, USA

ABSTRACT

Results are presented of a harmonic analysis of the large-scale cosmic-ray (CR) anisotropy as observed by the Milagro observatory. We show a two-dimensional display of the sidereal anisotropy projections in right ascension (R.A.) generated by the fitting of three harmonics to 18 separate declination bands. The Milagro observatory is a water Cherenkov detector located in the Jemez mountains near Los Alamos, New Mexico. With a high duty cycle and large field of view, Milagro is an excellent instrument for measuring this anisotropy with high sensitivity at TeV energies. The analysis is conducted using a seven-year data sample consisting of more than 95 billion events, the largest such data set in existence. We observe an anisotropy with a magnitude around 0.1% for CRs with a median energy of 6 TeV. The dominant feature is a deficit region of depth $(2.49 \pm 0.02 \text{ stat.} \pm 0.09 \text{ sys.}) \times 10^{-3}$ in the direction of the Galactic north pole centered at 189 deg R.A. We observe a steady increase in the magnitude of the signal over seven years.

Key words: cosmic rays – Galaxy: halo – ISM: magnetic fields – solar neighborhood – Sun: activity – supernova remnants

1. INTRODUCTION

Observation of the sidereal large-scale cosmic-ray (CR) anisotropy at energies of 1–100 TeV is a useful tool in probing the magnetic field structure in our interstellar neighborhood as well as the distribution of sources. CRs at these energies are almost entirely of Galactic origin and are expected to be nearly isotropic due to interactions with the Galactic magnetic field (GMF; Berezinskii et al. 1990). The gyro radii of CRs at these energies in a GMF of about 1 μG are from about 100 AU–0.1 pc which is much smaller than the size of the Galaxy. This has the effect of trapping the CRs in the Galaxy for times on the order of 10^6 years. Inhomogeneities in the GMF are interspersed randomly throughout the galaxy and in effect act as scattering centers for CRs. This randomizes their directions as they propagate leading to a high degree of isotropy on scales of a few hundred parsecs.

Anisotropy can be induced through both large scale and local magnetic field configurations which cause deviations from the isotropic diffusion approximation. At lower energies of around a TeV, the heliosphere may be able to induce a CR excess in the direction of the heliotail and also could modulate the overall CR anisotropy (Nagashima et al. 1989, 1998). At higher energies, the contribution of discrete CR sources has been shown to be capable of creating a large-scale anisotropy (Ptuskin et al. 2006; Strong et al. 2007).

Diffusion of CRs out of the Galactic halo can also produce an anisotropy. Since the matter density is higher in the Galactic disk compared to that in the surrounding halo, the diffusion coefficient will generally be much higher in the halo. For this reason, CRs produced in the Galactic disk will tend to diffuse out into the halo creating an anisotropy in the direction perpendicular to the disk. Predictions of the anisotropy have been made using values of the diffusion coefficient inferred using a given propagation model and observational data. This predicted anisotropy can take on values of 10^{-2} to 10^{-5} depending on the propagation model used (Berezinskii et al. 1990). Given this correlation between the anisotropy and diffusion coefficient, knowledge of the large-scale CR anisotropy can be used to constrain diffusion models.

In addition to the above effects, Compton and Getting introduced a theory (Compton & Getting 1935) of CR anisotropy which predicts a dipole effect due to the motion of an observer with respect to an isotropic CR plasma rest frame. The anisotropy arising from the Earth's motion around the sun is calculated to be on the order of 10^{-4} and would appear in universal time (UT). This effect has been observed by numerous experiments (e.g., see Aglietta et al. 1996; Amenomori et al. 2004). There is also a possible sidereal time (ST) anisotropy coming from the motion of the solar system through the Galaxy. This effect is more difficult to predict given that the isotropic CR rest frame is not known. Using the assumption that the CR

rest frame does not corotate with the Galaxy leads to a predicted anisotropy on the order of $\sim 0.1\%$. This effect has not been observed (Amenomori et al. 2006).

There have been numerous observations of the large-scale sidereal anisotropy in the range of energies 10^{11}–10^{14} eV. In this paper, we use large-scale anisotropy to refer to features of the anisotropy in the sky with an extent greater than $\sim 40°$ in right ascension (R.A.). Most of these observations are examined by fitting harmonics to the distribution of CR events in the R.A. direction. The main features of the anisotropy, the amplitude and phase, are fairly constant over the energy range mentioned above ($(3$–$10)\times 10^{-4}$ for the amplitude, and 0–4 hr for the phase, see Guillian et al. 2007 for a compilation). At TeV energies, the focus of this paper, the anisotropy is known to have a value on the order of 10^{-3} with a deficit region, sometimes called the "loss-cone," around $200°$ R.A., and an excess, or "tail-in" region, around $75°$ (Nagashima et al. 1989, 1998). In this paper, we present the results of a harmonic analysis of the large-scale CR anisotropy in the northern hemisphere as observed by the Milagro experiment.

2. THE MILAGRO OBSERVATORY

The Milagro observatory (Atkins et al. 2004) is a water Cherenkov detector which is used to monitor extensive air showers produced by TeV gamma rays and hadrons hitting the Earth's atmosphere. Milagro is located in New Mexico at a latitude of $35°.88$, a longitude of $106°.68$, and an altitude of 2630 m above sea level, possessing a large field of view of ~ 2 sr and a high duty factor of $>90\%$. The detector is composed of an 80 m $\times$ 60 m $\times$ 8 m pond filled with ~ 23 million liters of purified water and protected by a light-tight cover. The central pond is instrumented with two layers of photomultiplier tubes (PMTs): a top layer with 450 PMTs under 1.4 m of water which detects Cherenkov light from air shower electrons, electrons Compton scattered by gamma rays, and gamma rays that have converted to electron–positron pairs in the water; and a bottom layer with 273 PMTs 6 m under the surface used for gamma–hadron separation (not used in this analysis). The direction of an air shower is reconstructed using the relative timing of the PMTs hit in the top layer of the pond with an angular resolution of $< 1°$.

This pond is surrounded by a 200 m $\times$ 200 m array of 175 "outrigger" tanks. Each "outrigger" is a cylindrical, polyethylene tank with a diameter of 2.4 m and a height of 1 m. The outrigger tanks contain ~ 4000 liters of water and are instrumented with a single downward facing PMT located at the top of the tank. The inside of each tank is also lined with Tyvek (a white, reflective material) to increase the light collection capability of the PMT. The outrigger array, completed in 2003, is used to improve the angular resolution and in the estimation of primary particle energy.

The data used in this analysis were collected by Milagro from 2000 July through 2007 July. The hardware trigger was essentially a voter coincidence, requiring a multiplicity of about 75 PMTs. During this time the trigger multiplicity was tuned to maintain an average trigger rate of ~ 1700 events per second (to within 10%), the majority of which are due to hadronic showers. After event reconstruction, accepted events are required to have used at least 50 PMTs in the angular fit (N_{fit}) and have a zenith arrival angle of $\leqslant 50°$. The $N_{\text{fit}} \geqslant 50$ requirement removes effects due to fluctuations in the trigger threshold as events passing this cut generally have a higher PMT multiplicity than the hardware trigger requires. Although this makes the data more
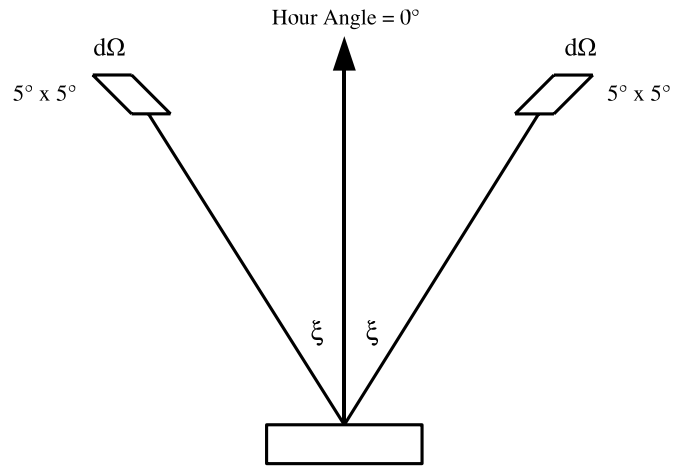
Figure 1. Diagram showing the definition of ξ used in the calculation of the FB asymmetry for a single declination band and a given 30 minute histogram. ξ is in the direction of hour angle. See the text in Section 3.1 for details.

stable, it also reduces the effective trigger rate to ~ 500 Hz. After these cuts the data set consists of 9.59×10^{10} CR events with a median energy of 6 TeV as determined from the measured primary CR spectra and simulated detector efficiency. The median energy varies slowly with zenith angle; it is 4 TeV for zenith angles from $5°$ to $10°$, and 7 TeV for zenith angles from $35°$ to $40°$.

Detector response to primaries is determined with a Monte Carlo simulation. This Monte Carlo has two main components: the simulation of an air shower in the atmosphere and the simulation of the shower through the Milagro detector. These simulations are carried out using the CORSIKA (Heck et al. 1998) and GEANT4 (Agostinelli et al. 2003) packages, respectively. CR nuclei ranging in mass from the dominant protons to those as heavy as iron are simulated according to their spectra as measured by the ATIC experiment (Panov et al. 2007). Because of the large shower-to-shower variations, Milagro cannot measure the energy of individual primaries generating these air showers without careful data selection criteria. Measurement of energy-correlated parameters does allow some determination of primary energy spectra without severely restricting the data. The energy analysis of the large-scale anisotropy will be the subject of a future publication.

3. DATA ANALYSIS

3.1. Forward–Backward Asymmetry and Harmonic Method

We have designed an analysis method to search for fractional deviations from isotropy down to levels of about 10^{-4}, below the level of predictions of the Compton–Getting (CG) effect and the magnitude of previous observations. Such sensitivity cannot be achieved by looking at raw event rates as a function of direction, because the air shower development essentially makes the atmosphere part of the detector, and weather effects lead to typical overall trigger rate variations of $\pm 15\%$. Thus, counting raw event rates would give random apparent anisotropies completely overshadowing a true signal. Instead, we employ the technique of forward–backward asymmetry (FB) using the number of events (N_F and N_B) collected in some small time interval in two "telescopes," i.e., pixels of small and equal solid angle, at the same forward and backward angle as shown in Figure 1.

$$FB = (N_F - N_B)/(N_F + N_B). \tag{1}$$
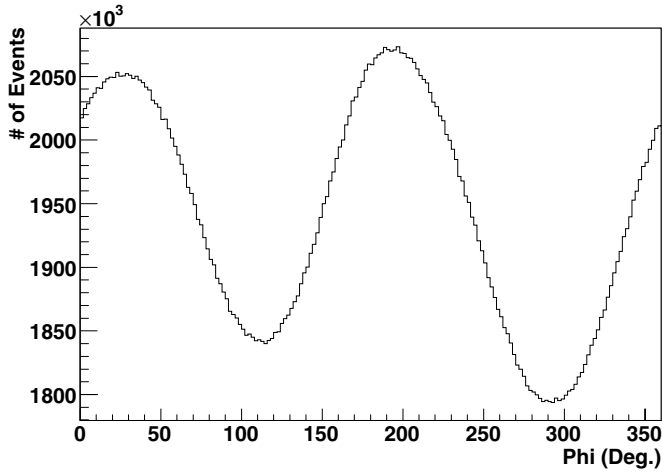
Figure 2. Representative plot of the number of events collected vs. azimuthal angle for the Milagro detector over the course of three days. The observed variation is the inherent geometric asymmetry in the detector which is at the level of ∼ 10%.

The expression of FB is manifestly independent of overall detector rate, as can be seen from the invariance of FB under the substitution $N_F, N_B \to cN_F, cN_B$, where c is a constant.

The analysis method utilizes the rotation of the Earth to search for a coherent modulation of FB during a 24 hour day. The FB modulation does not directly give the anisotropy of the sky, but is a function of it. As a region of the sky with an excess CR flux relative to the average (a positive anisotropy region) is swept into the forward "telescope," FB becomes more positive; when the same excess is swept into the backward "telescope," FB becomes negative. One can think of FB as a coarse "derivative" of the actual anisotropy of the sky. Thus, the FB modulation is a tool to obtain the quantity of interest, the fractional anisotropy (i.e., deviation from uniformity) of the sky, as detailed below.

The FB method is commonly used in particle physics (e.g., see Band et al. 1989) and is also closely related to the east-west technique, classically used in other anisotropy measurements (for an example see Nagashima et al. 1989), in which the ratio examined for modulation is $EW = (N_E − N_W)/N_{tot}$, formed with the rate integrated over the whole eastern and western sky. Again this is a rate independent quantity which is used to remove random fluctuations in overall detector rate, a common requirement in all experiments using the atmosphere as part of their detector. The EW method can be thought of as a single integrated measurement, compared to our multiple localized and independent measurements of FB which are used to improve the statistical power of this analysis.

Random daily weather-induced or instrumental variations of the anisotropy itself (and therefore of FB) are averaged out by summing (i.e., averaging) many full days, each sweeping a full circle in the sky. The random anisotropies decrease as $\sqrt{N_{days}}$ while a coherent signal is not reduced. Finally, because the method uses the time modulation of FB rather than FB itself, it is impervious to the inherent geometrical anisotropy present in the detector acceptance seen in the azimuthal distribution of Figure 2, which was observed to be stable during the lifetime of the experiment. We note that only instabilities of this geometrical anisotropy on the scale of a single day would affect the measurement, while a slow evolution would not.

Because this method measures the modulation in the direction of the Earth's rotation, it yields no information about the

modulation in the declination (decl.) direction. The results will therefore be for the projection of the anisotropy in the R.A. direction rather than the full two-dimensional anisotropy of the sky. Such a projection can be created for any visible decl. band. Since each decl. band sweeps around a full circle of the sky independently and contains statistically independent data, we choose to do separate analyses for each 5° decl. band of our data, considering each as a separate observation. Any theoretical description of the true two-dimensional anisotropy can be confronted with, or constrained by, our data (given in Section 4, Table 1) by projecting the anisotropy along R.A. in our decl. bands. In the rest of this paper we will always use the word anisotropy to mean this projected anisotropy.

To do the harmonic fit we make the assumption that the large scale anisotropy in any given decl. band can be modeled by a Fourier series and that it is a small modulation of a nearly isotropic signal. Three harmonics (the fundamental and the next two) have been found to be sufficient for this method (see Section 4.1). This allows us to see large scale effects having a width in R.A. of greater than ∼40°. In this harmonic model the normalized rate in a given direction of the sky, in celestial equatorial coordinates with decl. = δ and R.A. = θ (or the equivalent coordinate in the R.A. direction when using a different coordinate system) is:

$$\frac{R_\delta(\theta)}{\langle R_\delta(\theta) \rangle} = 1 + A_\delta(\theta) = 1 + \sum_{n=1}^{3} \gamma_{n,\delta} \cos n(\theta - \phi_{n,\delta}), \qquad (2)$$

where for a given δ the average in the denominator of the left side is over θ, and $A_\delta(\theta)$ is the fractional anisotropy in the R.A. direction. This model of the sky is complete once the six Fourier coefficients (three amplitudes and three phases) on the right side of the equation are known. The data analysis thus consists of determining these Fourier coefficients.

It is this harmonic model that allows us to connect the quantity of interest, namely the fractional anisotropy in the sky $A_\delta(\theta)$, and our chosen tool, the measurement of the modulation of the FB asymmetry. This connection is detailed explicitly below.

The quantity $N_{\theta_0,\delta}(\xi)$ is the number of CR events collected during a particular time interval (characterized by the angle θ_0), in an angular bin at a given decl. (δ) and local hour angle (ξ) characterizing the symmetric forward (+ξ) and backward (−ξ) inclination of the "telescope" of Figure 1. In this notation, the FB asymmetry of Equation (1) becomes

$$FB_\delta(\theta_0, \xi) = \frac{N_{\theta_0,\delta}(+\xi) - N_{\theta_0,\delta}(-\xi)}{N_{\theta_0,\delta}(+\xi) + N_{\theta_0,\delta}(-\xi)}. \qquad (3)$$

The bin counts are computed for half-hour intervals in ST, UT, and antisidereal time (AST; Farley & Storey 1954). These half-hour intervals are parameterized by an angle θ_0 which specifies the relative advance of the local meridian through the sky for the three different timescales:

$$\theta_0 = 3°.75 + 7°.5 \times IST$$
$$\theta_0 = 3°.75 + 7°.5 \times IUT$$
$$\theta_0 = 3°.75 + 7°.5 \times IAST$$

IST, IUT, and IAST are integers, from 0 to 47, denoting half-hour intervals of ST, UT, and AST (defined by flipping the sign of the transformation from UT to ST). In the above equations, the constants convert an integration time interval (half-hour) into degrees (7°.5) and a starting angle at the center of that interval.
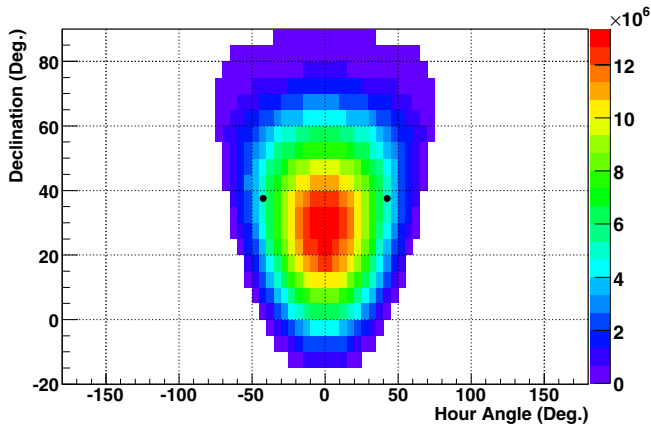
Figure 3. Example histogram showing the number of CR events vs. hour angle and decl. containing seven years of data for a single sidereal half-hour. The solid circles are an example pair of pixels shown in Figure 1 (with $\xi = 42°.5$) used in the calculation of the FB given by Equations (1) and (3).

In practice the CR events are recorded in histograms with $5° \times 5°$ bins according to their arrival direction from $-10°$ to $80°$ in decl. and $-50°$ to $+50°$ in hour angle. The events are collected over a 30 "minute" period giving us 48 half-hour histograms per day, where "minute" is defined in the three following time frames: sidereal (366.25 days yr^{-1}), universal (365.25 days yr^{-1}) and antisidereal (364.25 days yr^{-1}). The coordinate system in the ST frame is "sky-fixed," in the UT frame it is "sun-fixed," and in the antisidereal frame it is "nonphysical." Histograms for a given half-hour period are accumulated over any number of days to build an average set which corresponds to a chosen time period. A representative example is shown in Figure 3. These 48 half-hour histograms for the time frame, period, and decl. band of interest are then analyzed using the method of FB asymmetry described above combined with a harmonic fit.

Recognizing that $\theta = \theta_0 \pm \xi$, substituting Equation (2) for the harmonic sky model into Equation (3), and then utilizing $\gamma \ll 1$ and the appropriate trigonometric identities, we get

$$FB_\delta(\theta_0, \xi) \approx \sum_{n=1}^{3} -\gamma_{n,\delta} \sin(n\xi) \sin(n(\theta_0 - \phi_{n,\delta})). \quad (4)$$

Equation (4) is the prediction of the harmonic model of the sky, in terms of its Fourier coefficients, for the FB asymmetry, to be fit with our experimental data.

The next step is preparing the experimental data for the fit. For a fixed "telescope" angle ξ and at a given δ, we calculate FB and its statistical error by using the relevant pair of histogram bins in each of our 48 saved histograms of hour angle versus decl. (see Figure 3 for an example). Since we are only interested in the modulation of FB with θ_0 (i.e., with time), the average over all θ_0 is subtracted from the calculated FB. This step separates FB due to the inherent geometric anisotropy of the detector from the time modulated FB due to the sky anisotropy. These values are assembled into a 48 point, one-dimensional histogram of FB and its error versus θ_0 for this particular choice of ξ and δ. Equation (4) could be fit to this histogram to obtain the Fourier coefficients. But, this procedure can be done for several choices of ξ that we call ξ_i, each ξ_i is sampling the same sky, yielding a new FB versus θ_0 graph to fit. By choosing a set of ξ_i (where ξ_i ranges from $2°.5$ to a decl.-dependent maximum of up to $47°.5$ in $5°$ steps), centered on each of the $5° \times 5°$ pixels (see Figures 1 & 3) and calculating the FB (Equation (3)) with the
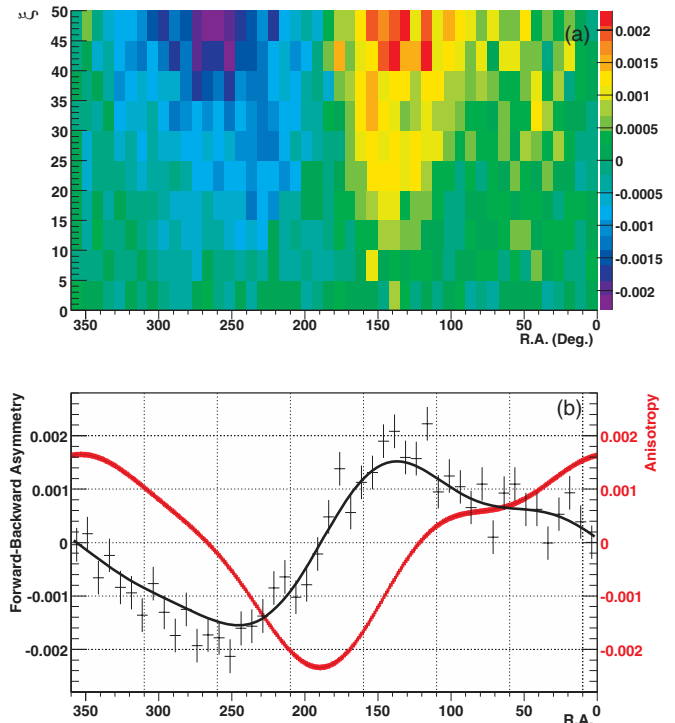
Figure 4. (a) Sample two-dimensional histogram of FB vs. ξ and R.A. for a single decl. band ($35°-40°$) calculated using Equation (3) for seven years worth of data (the binning reflects that the data is collected over half-hour intervals which are parameterized by θ_0). (b) Sample histogram showing the result of the two-dimensional fit of Equation (4) to (a) for a single slice in $\xi = 40°-45°$ (in black, left axis), and the reconstructed anisotropy of Equation (2) using the six Fourier coefficients obtained by the two-dimensional fit to (a) (in red, right axis).

contents of the corresponding pixels, we obtain up to 480 (48 values of θ_0 times up to 10 values of ξ_i) statistically independent measurements per decl. band. Every available pixel (histogram bin) pair in the 48 hour angle versus decl. histograms (Figure 3) is used once and only once. These one-dimensional histograms are assembled into a two-dimensional histogram of FB versus θ_0 and ξ_i. This histogram contains all our information about FB and its statistical error. The fit of Equation (4) to this two-dimensional histogram (a simultaneous fit over θ_0 and ξ_i) gives the experimental values and errors of the Fourier coefficients for the harmonic model of the anisotropy in a decl. band (Equation (2)). An example of the two-dimensional histogram that is being fit, and the result of the fit in θ_0 for a single slice in ξ_i are shown in Figures 4(a) and (b). The coherent signal in FB is clearly seen in both. Figure 4(b) also shows the resulting measured anisotropy reconstructed using the six fitted Fourier coefficients in this example.

The determination of the statistical errors on the Fourier coefficients is straightforward. The statistical errors on the number of events (N_F and N_B) are simply their square roots and these errors are propagated to the error on FB:

$$\sigma_{FB} = \sqrt{\frac{1}{N_F + N_B}(1 + FB^2)} \approx \sqrt{\frac{1}{N_F + N_B}}, \quad (5)$$

to a superb approximation. Since each FB bin in the two-dimensional histogram is statistically independent of the others, the fit is that of a two-dimensional experimental histogram with independent errors to the parameters of the theoretical function of Equation (4). This fit (using MINUIT James 2000)
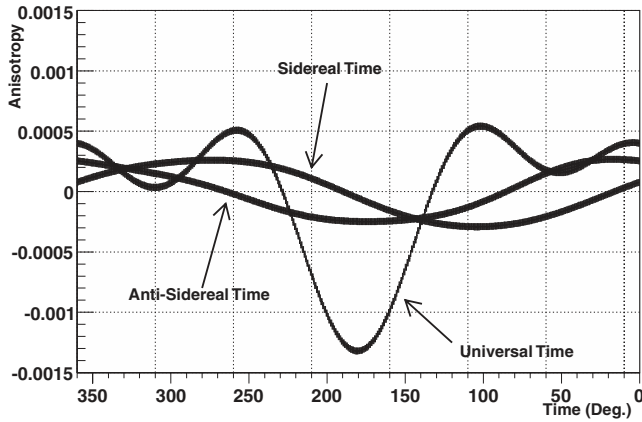
Figure 5. Results of an all-decl.-band anisotropy analysis using a MC generated UT signal. The signal consists of square well deficit from $150°$ to $210°$ in UT with an amplitude varying sinusoidally in time from 0.000 to 0.003. The signal seen in the ST and AST frames is induced by the UT time variation. The width of the curves reflects the statistical error.

Figure 6. Profiles in R.A. for individual $5°$ decl. bands from $10°$ to $50°$ used in the two-dimensional map seen in Figure 7. The width of the lines reflects the statistical error.

propagates the errors on the experimental data into errors on the parameters of the theory, namely the six Fourier coefficients of the anisotropy.

It is noted that the simultaneous fit of the different ξ_i bands is in effect an averaging over ξ_i which means that we are also averaging over any difference of energy in the data due to the dependence of atmospheric depth on ξ. This averaging is well justified after the fact by an examination of the ξ dependence discussed in Section 4.3.

Finally, we emphasize that the role of the FB asymmetry is over once the fit is done. The coefficients obtained are for the anisotropy of the sky, defined as the fractional difference of the rate at a given R.A. from its average over all R.A., for each decl. band. In Section 4.1, we tabulate the fit results for these 18 decl. bands, as well as graphically display their behavior.

3.2. Monte Carlo Tests of the Analysis Method

Tests of the analysis method were conducted using a Monte Carlo (MC) simulation that takes as input a two-dimensional map containing any desired anisotropy in UT or ST and then outputs events which can then be analyzed using the method discussed in the previous section.

We describe one important case in detail: a fixed UT signal will average to zero in ST or AST, but a seasonally modulated day–night anisotropy in UT will generate a false "sideband" signal in ST and AST. We use a time varying input in UT, where the magnitude of the UT signal varies sinusoidally between zero and its maximum with a period of one year, simulating an extreme seasonal variation. Figure 5 shows the results of an all-decl.-band analysis in three time frames for this test. The ST and AST frames, which have no input signal in the MC, show a clear signal induced by the time varying UT input. In this example the induced signal is at about half the amplitude of the UT time variation. The phases of the signals in ST and AST are different but their magnitudes are the same. Using this result we can estimate the systematic errors in the sidereal signal by examining the antisidereal signal. Since there are no physical processes which occur in the AST frame the signal should be zero when data sets of an integral number of years are used as seen from the MC checks above. Therefore, a signal present in the nonphysical AST frame is interpreted as being induced by variations in time of the UT signal and such a signal will also appear in the ST frame.
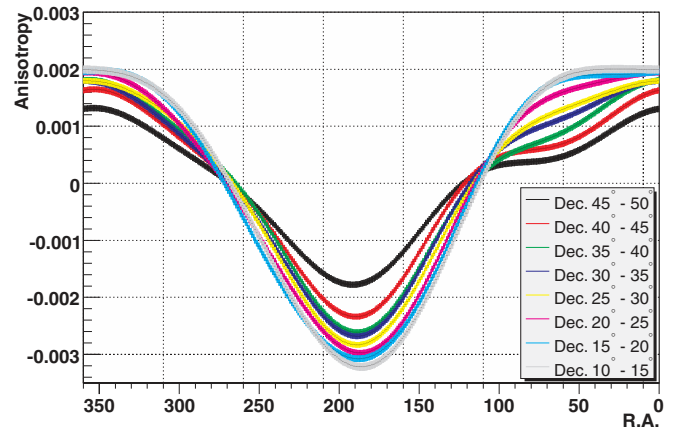
Two other sets of MC tests were successfully passed by the FB method. The first set tests the stability of the analysis method by using various simple signals (e.g., isotropic sky or the result of the analysis of real data) as input in ST with no input in UT or AST. Analysis of the output of these tests is consistent with the input within statistical errors. The UT and AST maps in these tests are consistent with isotropic as long as an integral number of years is used. This is to be expected since a static point in ST moves across the UT frame and returns to its original position after one year. In AST this point will move across two times in one year. Therefore when the decl. band is normalized a sidereal signal will average to zero in both UT and AST. This cancellation is of course also true for the sidereal sky with a signal fixed in UT (e.g., day, night effects).

The second set of tests shows that no false harmonic features are induced from isolated structures (e.g., a square well deficit centered around $\sim185°$ or the known Galactic equator excess of gamma rays; Atkins et al. 2005; Abdo et al. 2007, 2008). These tests show that no extra signals are induced except in the cases of a sharply discontinuous input and a time varying UT input. The discontinuous input induces features due to the use of only three harmonics as is expected from Fourier theory.

4. RESULTS

### 4.1. Multi-decl.-band Results and the Sidereal Sky Map

Table 1 is a summary of the harmonic-fit parameters for the sidereal sky fractional anisotropy obtained in each of 18 individual decl. bands. The χ^2 for the fit and the sample size in each decl. band is also listed in this table. Three harmonics were chosen as they give a better χ^2/ndf than one or two harmonics whereas there was little improvement in using four. Figure 6 displays the anisotropy profiles in R.A. for eight adjacent decl. bands in the table. As seen from the definition of the anisotropy in Equation (2), the profiles show the deviation from their average over all R.A., so that the area below and above the reference level of zero is the same: the existence of a deficit in some region implies an excess elsewhere.

Figure 7 assembles all 18 anisotropy profiles in their respective decl. positions into a two-dimensional color display of the local anisotropy, with red representing an excess and blue representing a deficit. Care must be taken in interpreting Figure 7. As explained before, our measurement is in the R.A. direction only, so that this picture does not purport to be the complete anisotropy

Table 1
Fit Parameters to the Sidereal Anisotropy for All 18 Declination Bands

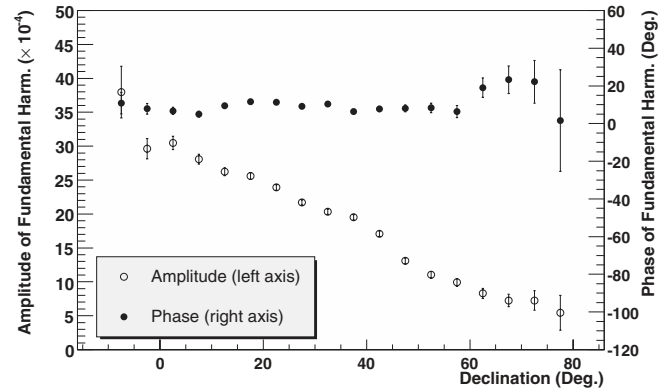| Decl.	Fundamental Harmonic		First Harmonic		Second Harmonic		χ^2/dof	Number
(mean)	Amplitude ($\times 10^{-3}$)	Phase (deg)	Amplitude ($\times 10^{-3}$)	Phase (deg)	Amplitude ($\times 10^{-3}$)	Phase (deg)		of Events ($\times 10^9$)
77.5	0.54 ± 0.26	2 ± 27	0.37 ± 0.14	13 ± 11	0.10 ± 0.11	−39 ± 19	262.57/234	0.65
72.5	0.73 ± 0.14	22 ± 11	0.19 ± 0.08	−25 ± 12	0.06 ± 0.06	11 ± 19	266.50/282	1.38
67.5	0.72 ± 0.09	23 ± 7	0.06 ± 0.05	−24 ± 26	0.01 ± 0.04	28 ± 116	308.67/330	2.39
62.5	0.83 ± 0.07	19 ± 5	0.12 ± 0.04	−65 ± 10	0.15 ± 0.04	−2 ± 4	355.61/330	3.63
57.5	0.99 ± 0.06	6 ± 3	0.12 ± 0.03	−42 ± 8	0.15 ± 0.03	3 ± 4	379.61/378	4.98
52.5	1.10 ± 0.05	8 ± 3	0.22 ± 0.03	−60 ± 4	0.17 ± 0.03	6 ± 3	406.42/378	6.31
47.5	1.31 ± 0.04	8 ± 2	0.33 ± 0.03	−63 ± 2	0.21 ± 0.02	2 ± 2	498.02/426	7.51
42.5	1.71 ± 0.04	8 ± 1	0.44 ± 0.02	−68 ± 2	0.26 ± 0.02	1 ± 2	475.85/426	8.46
37.5	1.95 ± 0.04	6 ± 1	0.45 ± 0.02	−73 ± 1	0.24 ± 0.02	3 ± 2	472.71/426	9.07
32.5	2.04 ± 0.04	10 ± 1	0.47 ± 0.02	−76 ± 1	0.20 ± 0.02	1 ± 2	520.47/426	9.28
27.5	2.17 ± 0.04	9 ± 1	0.53 ± 0.02	−78 ± 1	0.14 ± 0.02	0 ± 3	551.53/426	9.07
22.5	2.39 ± 0.04	11 ± 1	0.52 ± 0.02	−81 ± 1	0.12 ± 0.02	−12 ± 3	564.14/426	8.44
17.5	2.56 ± 0.05	12 ± 1	0.57 ± 0.03	−81 ± 1	0.10 ± 0.02	−32 ± 5	523.45/378	7.45
12.5	2.62 ± 0.06	9 ± 1	0.61 ± 0.03	−85 ± 2	0.05 ± 0.03	−28 ± 9	397.37/330	6.17
7.5	2.81 ± 0.07	5 ± 1	0.58 ± 0.04	−80 ± 2	0.08 ± 0.03	−39 ± 7	355.24/282	4.74
2.5	3.05 ± 0.10	7 ± 2	0.61 ± 0.05	−80 ± 3	0.14 ± 0.04	54 ± 5	280.00/234	3.31
−2.5	2.96 ± 0.15	8 ± 3	0.59 ± 0.08	−89 ± 4	0.23 ± 0.06	56 ± 5	271.14/186	2.04
−7.5	3.80 ± 0.38	11 ± 6	0.42 ± 0.19	−85 ± 13	0.14 ± 0.13	52 ± 18	118.02/90	1.04

Note. All quoted errors are statistical and are used in the calculation of χ^2.
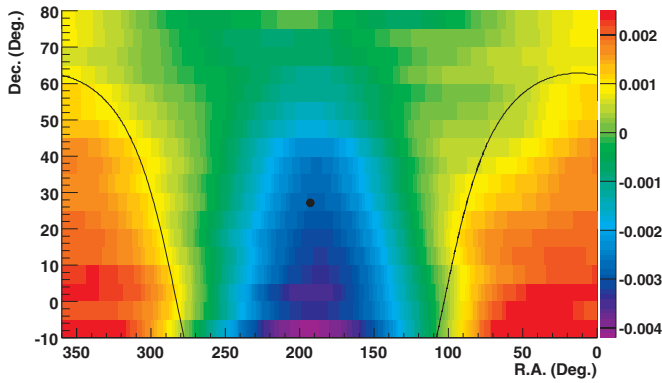
Figure 7. Result of a harmonic fit to the fractional difference of the CR rates from isotropic in equatorial coordinates as viewed by Milagro for the years 2000–2007. The color bin width is 1.0×10^{-4} reflecting the average statistical error. The two black lines show the position of the Galactic equator and the solid circle shows the position of the Galactic north pole. This map is constructed by combining 18 individual profiles of the anisotropy projection in R.A. of width 5° in decl. It is not a two-dimensional map of the sky. The median energy of the events in this map is 6 TeV.

Figure 8. Amplitude and phase of the fundamental harmonic obtained from a fit to seven years of data for each 5° decl. slice. The error bars are statistical.

of the celestial sphere; nor can the complete anisotropy be inferred from our results. Figure 7 is a two-dimensional display of one-dimensional information, the fractional anisotropy in R.A. What can be fairly compared across the decl. bands are the shape and strength of the fractional anisotropy in the R.A. direction; there is no information on the R.A.-averaged CR rate difference from one decl. band to another, i.e., the anisotropy in the decl. direction.

The data and their analysis are completely independent for each decl. band, but a striking commonality of the anisotropy behavior is seen in both Figures 6 and 7. Adjacent decl. bands have very similar profiles, in shape and in strength. The conclusion is that there is indeed a coherent anisotropy signal over a large swath of the sky. The dominant feature is a prominent valley or deficit region extending from 150° to 225° in R.A., and clearly visible in all decl. bands between −10° and

45°. The decrease of the depth of this valley, toward large values of decl., seen in the color picture of Figure 7, is explained at least in part by the fact that the circle in the celestial sphere generated by the Earth's rotation gets smaller and smaller, shrinking to a single point as decl. approaches 90°. The R.A. position of the valley minimum appears decl. independent in Figures 6 and 7. Figure 8 plots the amplitude and phase of the lowest harmonic versus decl., confirming both these trends; the amplitude is seen to decrease as decl. gets larger exhibiting the expected cos(decl.) dependence, while the phase is quite stable for decl. below 60°, where the amplitude is large enough for the phase to be well defined.

4.2. Single-decl.-band Results for ST, UT, and AST Time Frames

As a complement to the multi-decl.-band analysis of Section 4.1 we do a single-band analysis by projecting the hour angle versus decl. histograms onto the horizontal axis of Figure 3, thus integrating all decl. bands, then performing the same anisotropy analysis on this single band, to obtain the overall R.A. behavior. Examining the resulting single-band

Time Frame	Fundamental Harmonic		First Harmonic		Second Harmonic		χ^2/dof
	Amplitude $(\times 10^{-3})$	Phase (deg)	Amplitude $(\times 10^{-3})$	Phase (deg)	Amplitude $(\times 10^{-3})$	Phase (deg)	
Sidereal	1.994 ± 0.012	9.1 ± 0.4	0.400 ± 0.007	104.3 ± 0.5	0.118 ± 0.006	-0.9 ± 1.0	936.3/426
Universal	0.365 ± 0.012	217.4 ± 1.9	0.043 ± 0.007	168.7 ± 4.8	0.029 ± 0.006	93.2 ± 4.3	520.9/426
Antisidereal	0.120 ± 0.012	47.1 ± 5.8	0.019 ± 0.007	155.5 ± 11.1	0.013 ± 0.006	4.9 ± 9.4	425.9/426

Notes. All quoted errors are statistical and are used in the calculation of χ^2. For this single-decl.-band analysis, the systematic errors exceed the statistical ones.
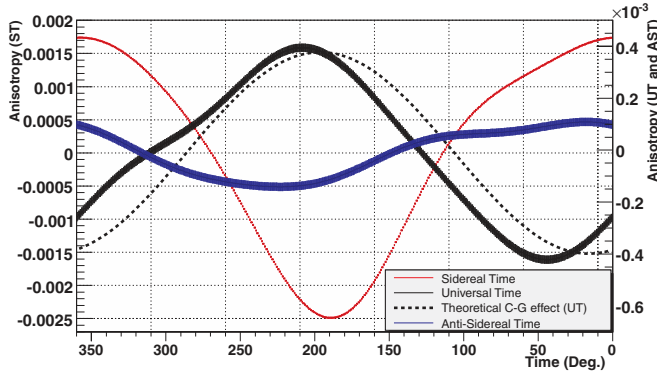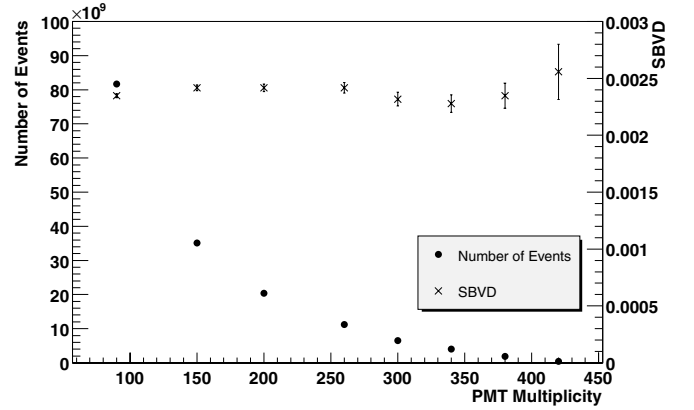

Figure 9. Anisotropy constructed by fitting a single projection containing data collected from all decl.'s collected over seven years in ST (red, left axis), UT (black, right axis) and AST (blue, right axis). The right axis (UT and AST) is expanded by a factor of 4 compared to the left axis (ST). The dashed curve is the predicted CG effect due to the Earth's motion around the sun which has an expected maximum value at 6 hr local solar time (196°.3 UT given the longitude of Milagro). In these plots the width of the curve reflects the statistical error.

Figure 10. Total number of events over a six-year period (left axis) and valley depth SBVD (right axis) vs. PMT multiplicity. The PMT multiplicity is defined as being the number of PMTs hit in the top layer of the pond for a given event. The lack of change in SBVD seen compared to the large decrease in the number of triggers shows explicitly the insensitivity of the analysis to variations in the trigger threshold.

anisotropy, with only six Fourier coefficients, gives a convenient and economical way to compare and contrast the behavior in all three coordinate systems corresponding to ST, UT, and AST. Table 2 gives the fitted harmonic-fit coefficients for ST, UT, and AST, and Figure 9 displays the resulting profiles for all three coordinate systems.

The sidereal-frame profile of Figure 9 clearly reproduces the dominant feature seen in the multiband analysis, the valley centered at 189° in R.A. The single-band valley depth (SBVD) is an alternate measure of the strength of the sidereal anisotropy and is found to be SBVD = $(2.49 \pm 0.02$ stat. ± 0.09 sys.$) \times 10^{-3}$, a 22.6σ signal. The method of systematic error estimation will be discussed in Section 4.3.

The CG effect due to the Earth's motion around the sun gives a predicted anisotropy in universal time frame which is a dipole (the lowest harmonic), plotted in Figure 9 together with our experimental result. Because the predicted signal amplitude is a factor of 5 smaller than the observed ST signal, and is correspondingly more susceptible to systematic distortions, this is a stringent test of the FB method. The experimental anisotropy profile is indeed dominated by the lowest harmonic as expected, has the predicted amplitude and reasonably close, though not in agreement (within errors) with the predicted phase. A detailed analysis of the UT measurement, including systematic errors, is deferred to a future publication. We consider our observation of the Earth-motion CG anisotropy signal in UT a powerful check of the analysis method, and thus a verification of the reliability of the result for the sidereal sky.

Since the antisidereal reference frame of Figure 9 is non-physical, we expect no real signal there, while systematic effect

distortions will show up in this frame also. Indeed this signal, plotted in Figure 9, is seen to be a factor of 3 smaller than the UT signal and thus a factor of 15 smaller than the ST signal. The observed AST signal will be used in the estimation of systematic errors in the next section.

4.3. Stability of Data and Systematic Errors

As a verification of the threshold independence and overall detector rate independence of the method and results, we raise the PMT multiplicity (the number of PMTs hit during an event in the air shower layer of the detector) requirement in the trigger from its hardware value of around 75 in several steps up to a value of about 400. Figure 10 shows the number of events and the fractional anisotropy valley depth SBVD as a function of the PMT multiplicity. The valley depth is seen to be stable over a factor of 5 in trigger threshold corresponding to a factor of ~ 25 in trigger rate. This is a direct confirmation that the result is indeed impervious to the detector rate and threshold, as expected from the rate cancellation of the FB method, explained in Section 3.1.

In Section 3.1 it is mentioned that the analysis method averages over different values of ξ, from 2°.5 to 47°.5. Figure 11 compares the single-band profiles when the full data set is split into two and analyzed separately, where one set contains data with ξ ranging from 0° to 25° and the other 25° to 50°. The good agreement of these two profiles demonstrates that the procedure of simultaneously fitting over all ξ is well justified.

To check for the possibility of a dependence on seasons, we break the data into three seasonal sets, defined as: April–
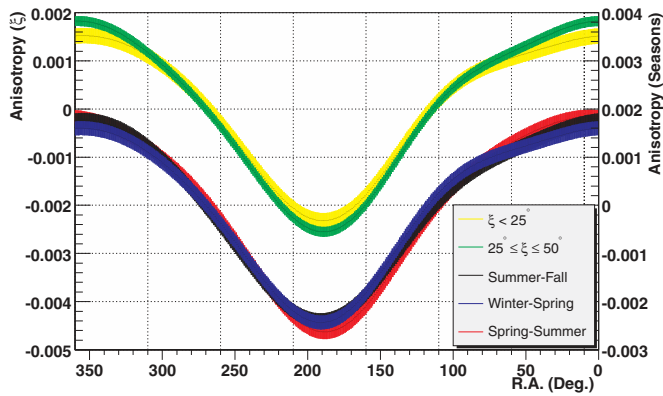
Figure 11. Single-decl.-band analysis showing seven years of data split into two sets: $\xi < 25°$ (in yellow), and $25° \leqslant \xi \leqslant 50°$ (in green). Also plotted is the seven years of data split into three seasonal sets: Summer–Fall in black, Winter–Spring in blue, and Spring–Summer in red. The error bars are statistical + systematic. The independence of the analysis on ξ as well as the lack of seasonal variation can be seen here.

July, July–November, and November–April corresponding to average local weather periods of: warm with low precipitation, high precipitation, and ice and snow, respectively. No significant changes are seen in Figure 11 which shows the three single-band profiles superimposed.

To test whether the observed ST signal is a sidereal phenomena and not due to UT effects, such as weather, we break the data into two-month periods. On these short timescales there will not be a cancellation between the ST, UT, and AST time frames since a fixed position in ST corresponds to a nearly constant position in UT. Figure 12 shows the position of the observed minima in UT for each two-month period over seven years. The solid line shows the expected position of a fixed sidereal minimum located at 189° R.A. If the minimum observed at 189° R.A. is a dominant feature of the sky, then the minimum in UT should follow the sawtooth pattern of the solid lines in the figure. If, on the other hand, there were dominant features in the UT sky, the positions of the minima should not correlate at all with this sawtooth pattern. The observed correlation between the observed and predicted positions of the minima in Figure 12 is a strong indication that the ST signal is the dominant feature in UT on this timescale. The same conclusion is reached when the corresponding analysis is carried out in the AST time frame where the sawtooth pattern has double the frequency.

To estimate systematic errors in ST or UT, for data sets of a full year (or several full years) of data, we use the anisotropy profiles in AST. The phase in the nonphysical antisidereal frame sweeps continuously between 0° and 360° in ST or UT in the course of a year, so that any coherent signal is lost because its phase is in effect randomized by this sweep. Since the physical signals have been washed out, what is left are any systematic distortions. We illustrate the logic and procedure for the case of the AST profile seen in Figure 9 for the single-band analysis. While the deviation of this profile from zero gives the possible magnitudes of the distortion of the valley depth, the phase relative to the signal in ST is unknown. If a deficit region of distortion in the AST profile were to coincide with the valley it would increase the valley depth SBVD, an excess would decrease it, and a zero crossing would leave it unchanged. We account for all these possibilities by projecting the AST curve of Figure 9 onto the vertical axis, to obtain the histogram shown in Figure 13 of all the possible distortions of SBVD that can result from this profile. We then take the rms deviation of this histogram, $\sigma_{\mathrm{rms}} = 0.09 \times 10^{-3}$
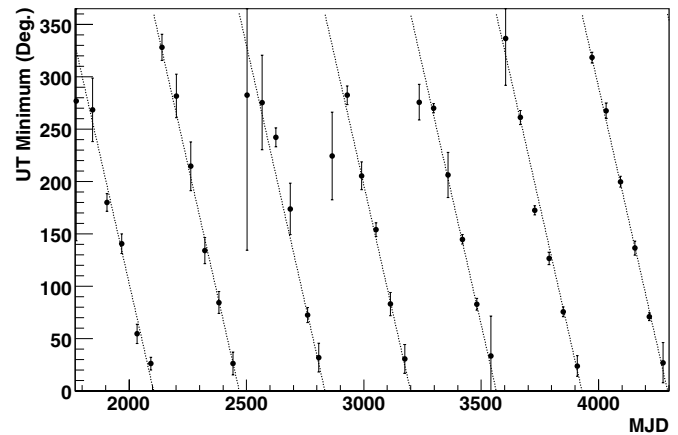
Figure 12. Position of minima in UT vs. Modified Julian Date (MJD) for data collected over the 42 two-month periods starting in 2000 July and ending in 2007 July. The error bars are the stat. errors. The solid line is the calculated position in UT of a constant sidereal position at R.A. equal to 189°. The excellent agreement between the data and the calculation shows that the UT signal is dominated by the ST signal.
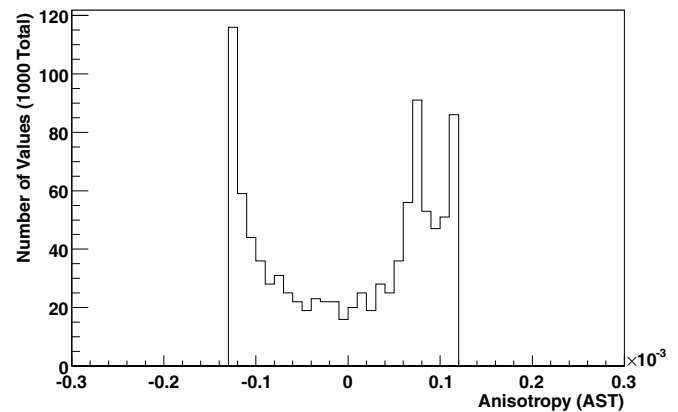
Figure 13. Histogram showing the projection of the AST curve from Figure 9 onto the anisotropy axis. The rms of this distribution is 0.09×10^{-3} which is used to determine the systematic error on the sidereal signal.
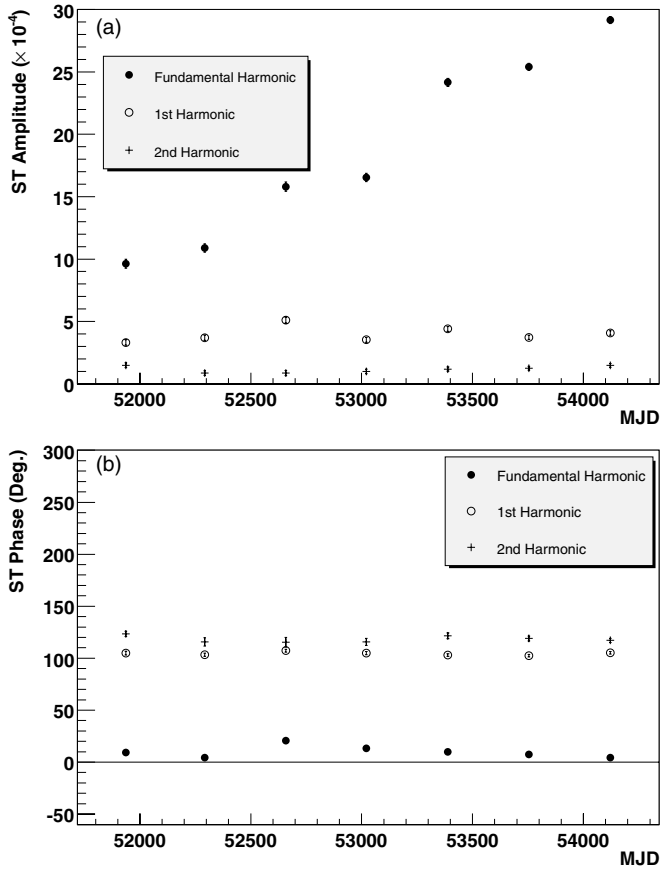
as the systematic error on the valley depth SBVD in the ST analysis.

4.4. Time Evolution of the Sidereal Anisotropy

To examine any time evolution of the anisotropy the data were split into seven-year-long sets from 2000 July to 2007 July. Figure 14 shows the three amplitudes and three phases obtained by fitting data from each yearly set using the single-band analysis (over all decl.). There is a stability in phase of all three harmonics over these seven years and in amplitude of the two higher harmonics. The fundamental harmonic, however, shows a clear increase in amplitude with time.

In order to quantify this increase in a precise manner, we look at the time evolution of the SBVD in the all decl. analysis, defined in Section 4.2 as a single-parameter measure of the strength of the anisotropy. Using this parameter allows us to include all three harmonics as well as utilize the systematic error estimation procedure outlined in the previous section. First we confirm that the valley is stable in position over time. The position in R.A. of the minima over the course of seven years shows very little variation as is expected from the stability of the harmonic phases seen in Figure 14. Fitting the position of the seven yearly minima to a constant yields a value of
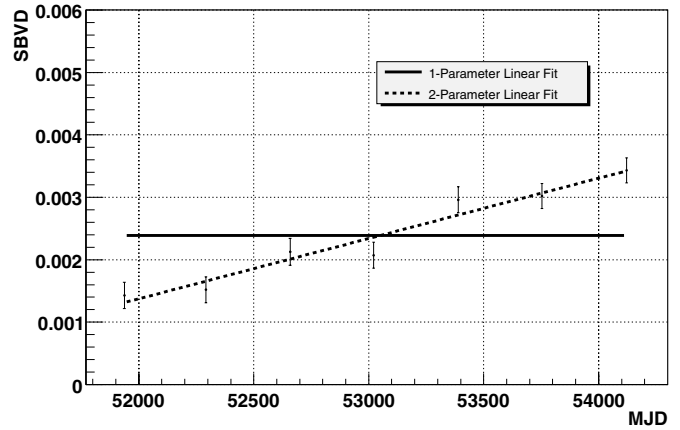
Figure 15. Valley depth in the all-decl.-band analysis (SBVD) vs. MJD for yearly sets from 2000 July to 2007 July. The error bars are the linear sum of the statistical & systematic errors. The solid line is the fit to a constant value and the dashed is the linear two-parameter fit. The $\chi^2/$ndf for the fits are 86.2/6 and 4.4/5 respectively. The fit parameter in the flat case is $(2.39 \pm 0.08) \times 10^{-3}$; the two fit parameters to the function $A(\text{MJD}) = p_0(\text{MJD} - 53000) + p_1$ are: $p_0 = (0.97 \pm 0.11) \times 10^{-6}$ and $p_1 = (2.34 \pm 0.08) \times 10^{-3}$.

Figure 14. (a) ST amplitudes of the three fit harmonics for the single-band (all decl.) analysis. (b) ST phases of the three fit harmonics for the single-band analysis. Both plots contain seven yearly data sets from 2000 July to 2007 July. The error bars are statistical.

$189° \pm 1°$ R.A. with a $\chi^2/\text{ndf} = 4.5/6$. This lack of change in position over time is what one would expect from an actual sidereal signal.
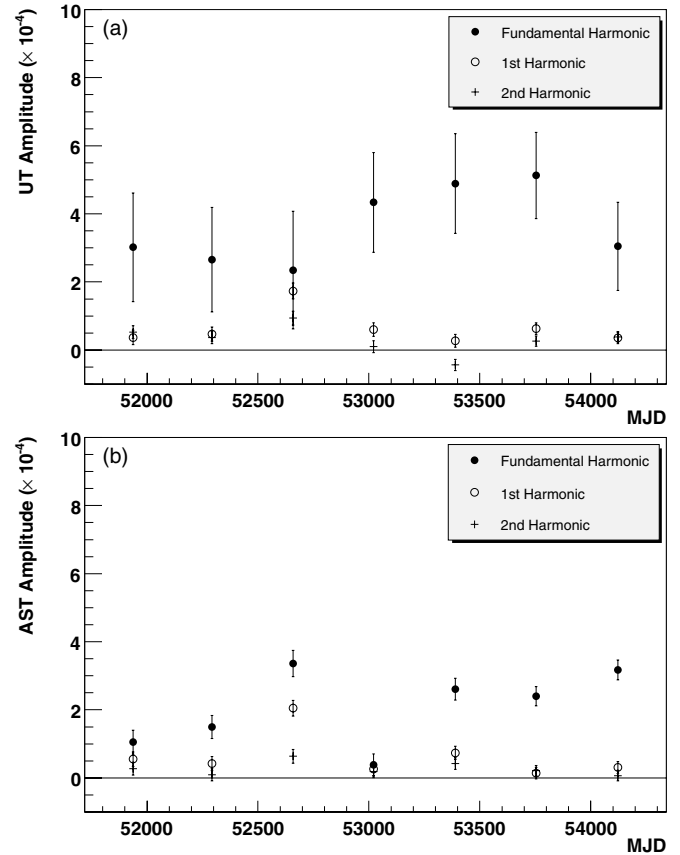
Figure 15, SBVD versus year, shows that there is strong evidence of a strengthening of the valley depth over the seven-year span of this data set.

To test the robustness of this time dependence a number of checks were done. As a test that is completely different from the insensitivity of anisotropy strength to trigger thresholds (described in Section 4.3 and Figure 10), we have done a direct check of whether the time-dependence of SBVD itself is threshold dependent. For several raised multiplicity thresholds between 90 and 280 PMTs hit in the top layer of the pond, the same time dependence is seen; the yearly trend does not disappear.

To see that this is a sidereal effect and not a detector effect we look at the yearly time evolution for the UT and AST signals. Figure 16 shows the amplitudes of the three fit parameters for the single-band analysis (all decl.) in both UT and AST; the Earth motion CG effect in UT should have no time dependence of the amplitude. The amplitudes of the harmonics in UT are constant over this seven-year data set, within the errors, as well as their phases (not shown in the figure). With respect to the amplitudes of the harmonics in AST, these appear to be significantly larger in some years, but even the largest amplitudes are 5 to 10 times less than those seen in ST. From these tests it thus appears that time dependent detector effects cannot account for the observed strong time dependence of the sidereal anisotropy.

Figure 16. (a) Universal time fit amplitudes for the single-band (all decl.) analysis for seven yearly data sets from 2000 July to 2007 July. (b) AST fit amplitudes for the single-band analysis for yearly data sets. For the UT fundamental harmonic only we show the statistical error + an estimate of the systematic error. For AST the error bars are only statistical. Note the lack of any definite trend, as opposed to what is seen in ST (Figure 14).

5. CONCLUSIONS

Previous experiments such as the Tibet Air Shower Array, with a modal energy of 3 TeV, and Super-Kamiokande-I, with a median energy of 10 TeV, have identified two coincident regions

of interest in their sidereal observations: an excess located at $\sim 75°$ R.A. or "tail-in" anisotropy, and a deficit at $\sim 200°$ R.A. or "loss-cone" anisotropy (Amenomori et al. 2006; Guillian et al. 2007). Both of these regions are consistent with Milagro observations. The "loss-cone" coincides with the deep central-deficit region seen in this analysis while the narrow "tail-in" excess is clearly observed in another Milagro analysis which is sensitive to features with extent smaller than $\sim 30°$ in R.A. (see Abdo et al. 2008 region A).

The strengthening of the signal in the central-deficit region over time is a result unique to this analysis. Tibet found no evidence of time variation comparing data split into two five-year periods, 1997–2001 and 2001–2005. However, only the second of these time periods overlaps with our data set for which the average value we observe in the deficit region agrees well with their measured deficit.

The anisotropy observed in the galactic cosmic rays could arise from a number of possible effects. The CG predicts that due to the motion of the solar system around the galactic center through the rest frame of the CR plasma an anisotropy is induced with the form of a dipole with a maximum in the direction of motion. For no corotation of the cosmic ray plasma with the Galaxy, the magnitude of the anisotropy is calculated to be 0.35% given our speed of ~ 220 km s^{-1}, while at the other extreme of full corotation, the anisotropy would be zero. No evidence of a Galactic CG anisotropy was seen in Amenomori et al. (2006). For no corotation, the dipole should have a maximum at R.A. $= 315°$ and decl. $= 48°$, and a minimum at R.A. $= 135°$ and decl. $= -48°$. Since our analysis method yields only a projection of the anisotropy the observed CG effect will be slightly different from the true effect. The CG effect we expect to see in this analysis was determined from Monte Carlo simulation and found to be a dipole with a maximum of 0.14% at $315°$ R.A. for the decl. range between $50°$ to $60°$. This range was considered to try to reduce effects from the central-deficit region. For the actual data, fitting a single harmonic to the projection in R.A. corresponding to decl.'s $50°$ to $60°$ gives a $\chi^2/\mathrm{dof} = 11505/998$ which is clearly a poor fit. Although this suggests that the observed anisotropy is not dominated by the galactic CG effect, its contribution to the anisotropy cannot be ruled out.

In addition to the CG effect there is expected to be an anisotropy stemming from the diffusion of CRs in the interstellar medium. At high energies the main effects are expected to be mainly due to the distribution of discrete CR sources and the structure of the galactic magnetic field in the neighborhood of the solar system. One study conducted consists of a simple diffusion model assuming increased production in the galactic disk due to supernova remnants (SNRs; Ptuskin et al. 2006; Strong et al. 2007). Also considered was the diffusion of CR out of the galactic halo. This is attractive since we have a deficit region in the general direction of the north Galactic pole which could be due in part to this diffusion. The main contribution of CR from SNRs was considered for sources with distances from Earth of < 1 kpc and ages < 0.05 Myr. Calculations performed (Ptuskin et al. 2006; Strong et al. 2007) using these sources and taking into account CR re-acceleration as well as diffusion out

of the galaxy gives an anisotropy about 3 times greater than observed, with the main source of the anisotropy due to the Vela SNR located at $128°$ R.A. and $-45°.75$ decl. This model only predicts the magnitude of the expected anisotropy, not its exact phase. It also is remarked that this is a simplified model which assumes an isotropic diffusion tensor which is not explicitly known to be true at these energies.

At energies of ~ 1 TeV the heliosphere is believed to have an influence on the distribution of CR (Nagashima et al. 1989, 1998). One possible reason for the modulation of the anisotropy on the observed timescale could be due to variations in the heliosphere since we know that it changes in relation to solar output. It is noted that our data begins at the solar maximum and ends near the solar minimum. A recent derivation of the diffusion tensor contains a new component due to perpendicular spatial diffusion which is expected to be an important factor in understanding the anisotropy due to the Galactic disk as well as the modulation of CR in the outer heliosphere (Schlickeiser et al. 2007). Finding a consistent explanation of the observed anisotropy and especially its time evolution will be a challenge.

REFERENCES

Abdo, A. A., et al. 2007, ApJ, 664, L91
Abdo, A. A., et al. 2008, ApJ, 688, 1078
Abdo, A. A., et al. 2008, Phys. Rev. Lett., 101, 221101
Aglietta, M., et al. 1996, ApJ, 470, 501
Agostinelli, S., et al. 2003, Nucl. Instrum. Methods, A506, 250
Amenomori, M., et al. 2004, Phys. Rev. Lett., 93, 61101
Amenomori, M., et al. 2006, Science, 314, 439
Atkins, R., et al. 2004, ApJ, 608, 680
Atkins, R., et al. 2005, Phys. Rev. Lett., 95, 251103
Band, H. R., et al. 1989, Phys. Lett. B, 218, 369
Berezinskii, V. S., Bulanov, S. V., Dogiel, V. A., & Ptuskin, V. S. 1990, Astrophysics of Cosmic Rays (Amsterdam: North Holland)
Compton, A. H., & Getting, I. A. 1935, Phys. Rev., 47, 817
Farley, F., & Storey, J. 1954, Proc. Phys. Soc. A, 67, 996
Guillian, G., et al. 2007, Phys. Rev. D, 75, 062003
Heck, D., Knapp, J., Capdevielle, J. N., Schatz, G., & Thouw, T. 1998, Forschungszentrum Karlsruhe Report, FZKA, 6019
James, F. 2000, MINUIT: Function Minimization and Error Analysis, Reference Manual (Geneva, CH: CERN), http://wwwasdoc.web.cern.ch/wwwasdoc/minuit/minmain.html
Nagashima, K., Fujimoto, K., & Jacklyn, R. M. 1998, J. Geophys. Res., 103, 17429
Nagashima, K., et al. 1989, Nuovo Cimento C, 12, 695
Panov, A. D., et al. 2007, Bull. Russ. Acad. Sci., Phys., 71, 494
Ptuskin, V. S. , Jones, F. C., Seo, E. S., & Sina, R. 2006, Adv. Space Res., 37, 1909
Schlickeiser, R., Dohle, U., Tautz, R. C., & Shalchi, A. 2007, ApJ, 661, 185
Strong, A., Moskalenko, I., & Ptuskin, V. 2007, Annu. Rev. Nucl. Part. Syst., 57, 285